Ceramics International 46 (2020) 9446–9454

Contents lists available at ScienceDirect

Ceramics International

journal homepage: www.elsevier.com/locate/ceramint

Connecting theory with experiment to understand the photocatalytic activity of CuO–ZnO heterostructure

M.C. Oliveira[a,*], V.S. Fonseca[a], N.F. Andrade Neto[a], R.A.P. Ribeiro[b], E. Longo[b], S.R. de Lazaro[c], F.V. Motta[a], M.R.D. Bomio[a]

[a] *LSQM – Laboratory of Chemical Synthesis of Materials, Department of Materials Engineering, Federal University of Rio Grande Do Norte, P.O. Box 1524, 59078-900, Natal, RN, Brazil*

[b] *CDMF-LIEC, UFSCar, P.O. Box 676, 13565-905, São Carlos, SP, Brazil*

[c] *Department of Chemistry, Universidade Estadual de Ponta Grossa, Av. General Carlos Cavalcanti, P.O. Box 4748, 84030-900, Ponta Grossa, PR, Brazil*

ARTICLE INFO

Keywords:
n-ZnO/p-CuO heterostructure
DFT
Photocatalysis
Methylene blue dye

ABSTRACT

Semiconductor based photocatalysis attracts wide attention because of its ability to directly utilize solar energy to degrade pollutants and convert energy, with heterojunction photocatalysts being good candidates for superior activity due to the spatial separation of photogenerated electron–hole pairs. Herein, CuO/ZnO heterostructures were successfully synthesized by a microwave-assisted hydrothermal method, with the structure, electronic and photocatalytic properties analyzed by means of experimental and theoretical methods. The X-ray diffraction patterns revealed that a CuO/ZnO heterostructure was formed, while FE-SEM analysis indicates the role of different morphologies for CuO, ZnO and CuO/ZnO heterostructures. The solar-driven photocatalytic measurements combined with DFT calculations indicate that CuO, as a p-type and narrow band-gap sensitizer, can make the n-type ZnO respond to visible light and promote the separation of photogenerated charge carriers by building a p-n heterogeneous structure. As a result, the CuO/ZnO heterostructure shows good promise for solar-driven photodegradation.

1. Introduction

Binary metal oxide semiconductors have been extensively used as sensors, catalysts, adsorbents, piezoelectric devices, conductor materials, fuel cells, solar cells [1–11], etc. Among various metal oxide semiconductors, researchers have paid more attention to CuO/ZnO heterojunction due to their interesting properties such as natural p-n characteristics, high sensitivity to humidity changes, the fast dynamic response, and broad light absorption [8,12–14].

In view of photocatalytic applications, Zinc–Copper composite shows excellent performance in photocatalytic degradation of organic dyes such as methylene blue [15]. Methylene blue (MB) is a color cationic used as a traditional dye for painting cotton, wool, and silk [16–21]. Coupled semiconductor materials have two types of energy levels which play an important role in achieving charge separation. Coupling different semiconductor oxides can reduce the band gap, extending the absorbance range to a visible region which leads to electron–hole pair separation under irradiation and consequently achieving superior photocatalytic activity [22,23]. Recently, ZnO has been blended with various other metal oxides such as; TiO_2, SnO_2, MgO, CuO, Cu_2O, etc. [24–28], displaying higher degradation of organic pollutants [29].

Zinc oxide (ZnO) is a typical n-type metal oxide semiconductor with a band gap of 3.37 eV, showing a high specific energy density, as well as superior electrical, piezoelectric and optoelectronic properties [30–35]. ZnO-based nanocomposites have exhibited enhanced photocatalytic properties which partly result from the different crystallites or electronic coupling between ZnO and the other phase of the composite. Copper Oxide (CuO), a narrow band gap of 1.2 eV [36] and p-type semiconductor which enables wide application in photocatalytic and solar cells, as well as in electrochemical, field emission and catalysis applications [37–39] has been selected to fabricate CuO/ZnO p-n heterojunction by a facile method of synthesis called Microwave-Assisted Hydrothermal (MAH) [39–43].

Based on the above considerations, in this work we report a combined theoretical and experimental investigation of CuO/ZnO heterojunctions as a promising material in photocatalytic activity in which we seek to fulfill a four-fold objective. The first is to report the novel synthesis of pure and surfactant-assisted (ethylenediamine, EDA, $C_2H_4(NH_2)_2$) CuO and posteriorly to synthesize the ZnO through the

* Corresponding author.
E-mail address: marisa-coliveira@hotmail.com (M.C. Oliveira).

https://doi.org/10.1016/j.ceramint.2019.12.205
Received 26 November 2019; Received in revised form 22 December 2019; Accepted 24 December 2019
Available online 25 December 2019
0272-8842/

Pechini method, and finally obtain a CuO/ZnO heterostructure by employing the MAH technique. This synthesis method has received special attention due to its various advantages including normal atmospheric pressure reacting, short reaction time, rapid heating, low reaction temperature, homogeneous thermal transmission, and phase purity with a better yield [44–46]. Secondly, X-ray diffraction (XRD), *ultraviolet* and *visible (UV–Vis)* absorption *spectroscopy* in combination with field-emission scanning electron microscopy (FE-SEM) and Rietveld refinements were employed to characterize the samples and determine the effect of their chemical composition on the photocatalytic degradation of MB. The third aim is to investigate the geometry, electronic and vibrational properties of ZnO and CuO materials using the Density Functional Theory (DFT). Lastly, the fourth objective is to apply a joint experimental and theoretical strategy to obtain an explanatory mechanism for the photocatalytic p-n heterojunction. Based on these results, we provide additional insights about the superior solar-driven photocatalytic activity for the degradation of MB using CuO/ZnO heterostructure. We believe that these novel results are of significant relevance since they may inspire efficient synthesis of these and other related metal oxide semiconductors and provide critical information to expand our fundamental understanding of photocatalytic activity.

2. Experimental and computational details

2.1. Materials

Copper(II) nitrate hydrate, ($Cu(NO_3)_2.2.5H_2O$, 98%, Alfa Aesar), potassium hydroxide, (KOH, 99%, Synth), ethylenediamine, (EDA, $C_2H_4(NH_2)_2$, 99%, Vetec), zinc nitrate hexahydrate, (Zn(NO3)2.6H2O, 98%, Sigma Aldrich), ethyleneglycol, (EG, $C_2H_6O_2$, 99%, Synth), and citric acid ($C_6H_8O_7$, 99.5%, Synth) were used to prepare the p-CuO/n-ZnO heterostructure.

2.2. Preparation of p-CuO/n-ZnO heterostructure

First, CuO nanoparticles were synthesized by the MAH method. To do this, 2.2 g of copper nitrate was kept under magnetic stirring in 80 mL of deionized water. After complete homogenization, KOH was added to set the reaction pH to 10. The solution was then placed in a Teflon reactor and inserted into the autoclave where it was heated to 140 °C and remained for 30 min. After this period, the supernatant was washed with deionized water and centrifuged to remove residual ions and neutralize the pH. The precipitated material was then dried at 100 °C for 24 h. Synthesis using EDA surfactant occurred similarly, where 3 mL EDA was added before KOH.

Zinc oxide (ZnO) particles were obtained by the Pechini method. To do this, 13.83 g of $C_6H_8O_7$ was dissolved in 60 mL of deionized water and kept under magnetic stirring at 70 °C. After 10 min, 7.13 g zinc nitrate was added and stirred for a further 10 min. Next, 8.28 mL of EG was added to obtain a resin. The resin was pre-calcinated in a furnace, and remained for 2 h under 350 °C. After this, the material was macerated and calcined at 700 °C for 2 h.

The heterostructure was obtained similarly to CuO powders with EDA, for which 2.2 g of copper nitrate, 0.5 g of ZnO powders and 3 mL of EDA was kept under magnetic stirring in 80 mL of deionized water. KOH was added to set the reaction pH to 10 and the solution was then placed in a Teflon reactor in the autoclave where it was heated to 140 °C and remained for 30 min. The supernatant was washed, centrifuged and dried for 24 h under 100 °C.

2.3. Characterization

X-ray powder diffraction (XRD) was employed to determine the phase composition and crystal structure of the as-synthesized CuO/ZnO heterostructure. The measurements were carried out using a Shimadzu XRD-6000 diffractometer, scanning from 20 to 80° at a speed of 1°/min and 0.02° step using CuKα radiation (1.5418 Å). The morphology was observed using field emission scanning electron microscopy (FE-SEM – Supra 35 Zeiss) and the chemical mapping was performed on a ZEISS SmartEDX. The band-gap (E_{gap}) of metal oxides were estimated by ultraviolet–visible (UV–Vis) absorption spectra of the annealed samples which were obtained in total diffuse reflectance mode using a Shimadzu Spectrophotometer UV-2550. The E_{gap} region was determined applying the Wood and Tauc function [47]. All measurements were performed at room temperature.

2.4. Photocatalytic activity

The photocatalytic activity was estimated against methylene blue (MB) dye at pH 5. To do this, 0.05 g of the material was placed in contact with 50 mL of the MB aqueous solution (cationic, 10^{-5} mol L^{-1} concentration) and kept under stirring for 120 min to eliminate the adsorbent effects. After this time, the solutions were exposed to sunlight (initially at 10 o'clock a.m., with the highest solar incidence of IUV 10) for 80 min. The temperature of the solutions was monitored throughout the test, remaining at around 27 °C and an aliquot of 2 mL was taken every 20 min and placed in a Shimadzu UV-2600 spectrophotometer for analysis of the absorbance band. The photocatalytic activity was then determined by comparing the aliquot absorption bands with the initial band. All weather data were collected from the *Instituto Nacional de Pesquisas Espaciais* (*INPE*).

2.5. Computational details

Density functional theory (DFT) calculations for both p-CuO and n-ZnO oxides were performed within the linear combination of atomic orbitals approach, as implemented in the CRYSTAL17 code [48]. Cu, Zn and O atoms were described by the atom-centered all-electron 86-411d41G, 86-411d31G8-411d1GGaussian basis set, respectively [49–51]. Despite the common semiconductor behavior observed for n-ZnO, tenorite p-CuO behaves as a Mott insulator, constituting a challenging topic regarding the representation of its electronic structure by first-principle methods [52,53]. Therefore, the hybrid B1WC functional method was employed in all calculations for treating the exchange and correlation effects, as based on previous theoretical calculations where the referred functional method shows the best performance along a set of exchange-correlation treatments for the strongly-correlated CeO_2 and Ce_2O_3 materials [54,55]. Thus, analyses of the electronic properties in terms of Density of States (DOS) and Band Structure profiles was carried out.

Electronic integration was performed using a dense $8 \times 8 \times 8$ Monkhorst-Pack [56] *k*-mesh for the pristine and defective cells, containing 150 and 50 *k*-points for p-CuO and n-ZnO, respectively. The accuracy of the Coulomb and exchange integral calculations were controlled by five thresholds set to 8, 8, 8, 8, and 16. The convergence criterion for mono- and bi-electronic integrals were set to 10^{-8} Ha, while the root-mean-square (RMS) gradient, RMS displacement, maximum gradient, and maximum displacement were set to 3×10^{-5}, 1.2×10^{-4}, 4.5×10^{-5}, and 1.8×10^{-4}a.u., respectively. Both lattice parameters and atomic positions were relaxed in all cases.

The vibrational frequencies were obtained at the Γ point in order to verify that all investigated geometries correspond to stationary points in the potential energy surface. In this case, the harmonic approximation was implemented computing the dynamic matrix by the numerical evaluation of the first derivative of analytical atomic gradients [48].

3. Results and discussion

The crystallographic structures of all synthesized CuO (pure and 3 mL EDA) and ZnO structures and the p-CuO/n-ZnO heterostructure were characterized by powder X-ray diffraction, and are shown in Fig. 1.

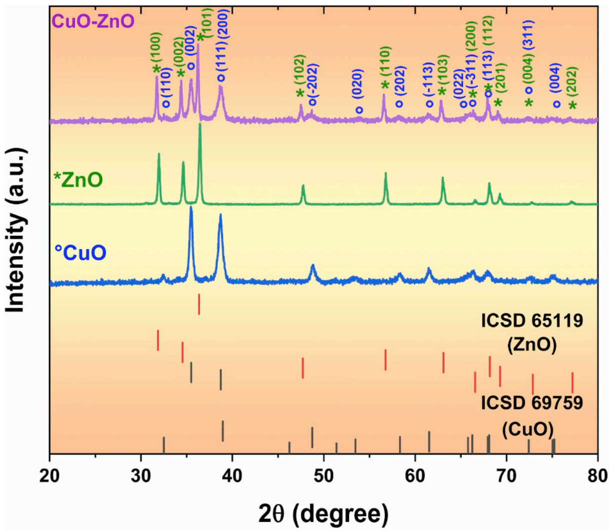

Fig. 1. XRD pattern of copper oxide (CuO) samples, ZnO nanostructure and CuO/ZnO heterostrucure prepared by the MAH method.

Fig. 1 shows XRD spectra of the CuO, ZnO pure structures and the CuO/ZnO heterostructure. The diffraction peaks of CuO were in agreement with the reference pattern of monoclinic structure (ICSD N° 69759) [57–59]. The crystal phase of ZnO particles was determined as a hexagonal wurtzite structure which can be indexed on the basis of ICSD No. 65119 [14,60]. The hexagonal wurtzite structure can be identified for the (100), (002), (101), (102), (110), (103), (200), (112), (201), (004) and (202) planes, as illustrated in Fig. 1. The observed diffraction peaks for both samples are well-defined, revealing that the powders had good crystallinity.

It is important to point out here that the addition of ethylenediamine (EDA) as a surfactant to copper oxide synthesis had the objective of influencing the dispersion, size control and final nanoparticle morphology. FE-SEM micrographs of the nanostructure CuO pure and EDA synthesized by MAH at 140 °C for 30 min are shown in Fig. 2(a-b), while ZnO and CuO/ZnO heterostructure morphologies are presented in Fig. 2c-d.

Fig. 2a showed a large quantity of CuO plates with an agglomerated and polydispersed nature, constituting the leaf-like nanopatches in morphology. Similar results were reported by other authors, showing that sea urchin-like morphology is a generic feature of CuO growth under MAH conditions [57]. Moreover, as appointed by L. Xu et al. [61], CuO with different morphologies have been successfully synthesized through different methods such as nanoellipsoids, nanoribbons, nanorods, nanotubes, nanorings, nanosphere, nanocages, hollow microsphere, microflower, aligned nanowires, and dandelion. Fig. 2b indicates the morphology of the sample after the incorporation of EDA (3%) into CuO showed an apparently modified architecture, exhibiting an increase in crystallite size from 21.51 nm to 59.91 nm, as obtained by using the Scherrer equation [62] according to the broadening diffraction peak in the XRD. Furthermore, the final morphology formation can be described as a fusion of CuO planes during the crystal growth process. In the sample with the addition of 3 mL of EDA, a nanoflower morphology growth occurred via a non-oriented attachment, which resulted in obtaining a greater number of agglomerated plates in relation to pure plates.

Fig. 2c additionally indicates that ZnO particles were formed showing a non-uniform and irregular shape. Compared to pure (irregular plates) and EDA-assisted (flowers) CuO, as well as for ZnO (irregularly shaped and non-uniform), the final morphology of the CuO/ZnO heterostructure is composed of flower-like nanostructures and some non-uniform and irregular shapes growing on the structures, as presented in Fig. 2d.

Mapping the distribution of the atoms for the formation of the CuO/ZnO heterostructure can be illustrated, as shown in Fig. 3a-c, where it is possible to observe the regions of interfacial contact between the two oxides in the formation of the CuO/ZnO heterostructure. This fact is in accordance with Taraka et al. [63], in which the CuO/ZnO heterostructure is confirmed by the interface between ZnO and CuO particles through the corresponding (111) plane of CuO, along with the (101) plane of ZnO. Therefore, such evidence clearly reveals the fused geometry in the CuO/ZnO heterojunction nanostructure.

Let us now briefly analyze and discuss the electronic structure of a synthesized CuO pure structure with 3 mL EDA, a ZnO pure structure and a CuO/ZnO heterostructure. To do this, Fig. 4 shows the UV–Vis spectra of the mentioned materials which can help in determining the E_{gap} values.

Fig. 4 shows the absorption curves obtained by the proposed Kubelka-Munk [64] method and their corresponding E_{gap} energies

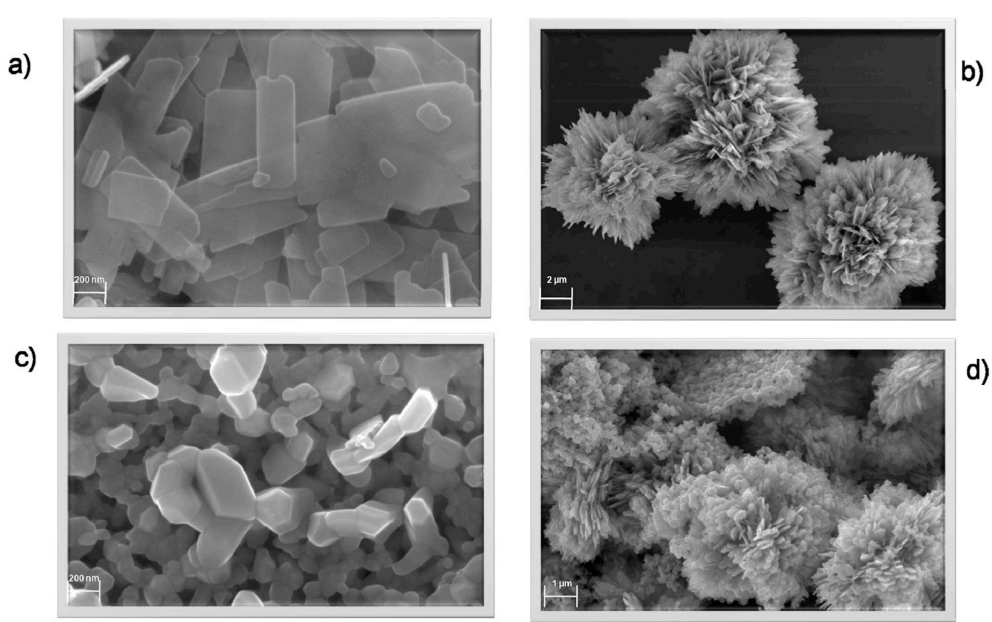

Fig. 2. FE-SEM micrographs: **(a)** CuO pure, **(b)** CuO with 3 mL of EDA, **(c)** ZnO pure nanostructure and **(d)** CuO/ZnO heterostructure.

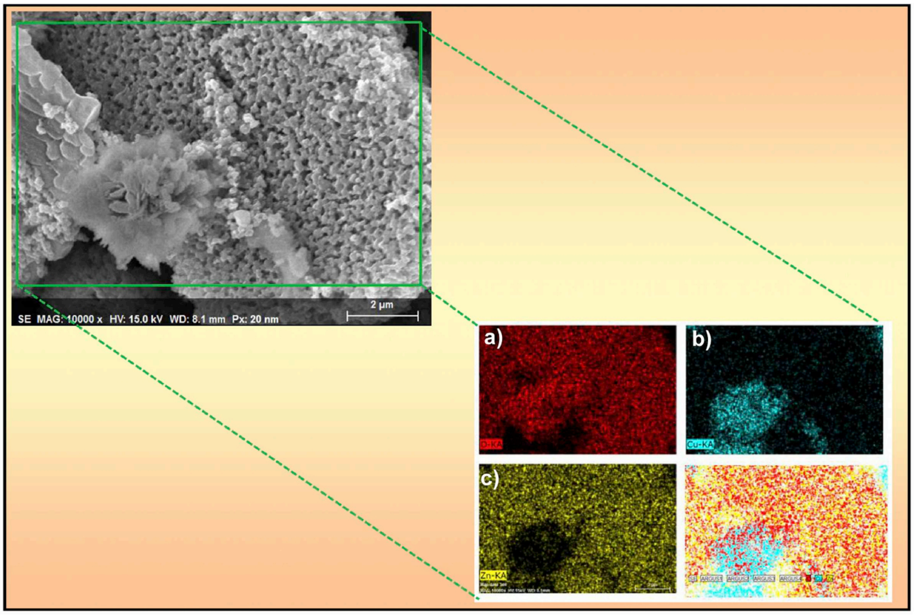

Fig. 3. Area and chemical mapping for the CuO with 3 mL of EDA and ZnO oxides of the heterostrucure. In the mapping, **(a)** oxygen is represented in red, **(b)** copper is represented in blue and **(c)** zinc is represented in yellow.

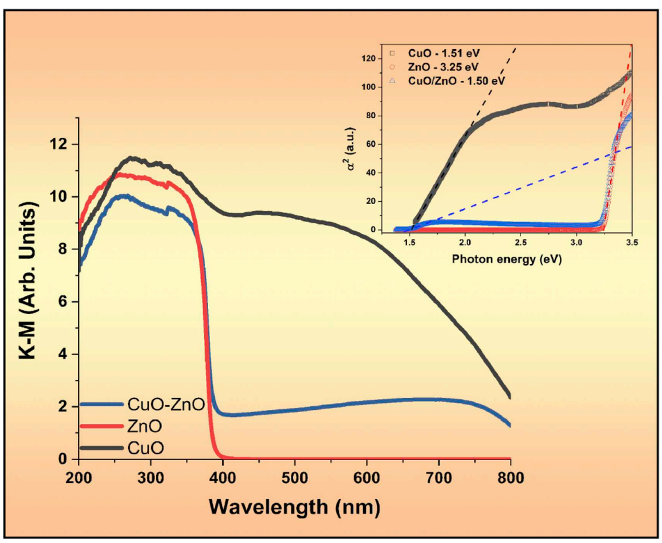

Fig. 4. UV–Vis spectra of representative CuO, ZnO and CuO/ZnO bandgap analyses.

obtained by the Wood and Tauc methodology using the direct permissible transition. In this case, it was observed that ZnO only shows absorption in the ultraviolet region, while CuO shows absorption throughout the visible spectrum, as well as for the CuO/ZnO heterostructure. The E_{gap} values were calculated as 1.51 eV for CuO and 3.25 eV for ZnO. Two characteristic transitions were observed in the CuO/ZnO heterostructure, with the smallest corresponding to an E_{gap} value of 1.50 eV. These values showed good agreement with previous reported experimental results [65–67].

The photocatalytic activity of the CuO, ZnO and CuO/ZnO heterostructures were evaluated by examining the photo-assisted degradation of MB dyes under sunlight radiation for 80 min, and are shown in Fig. 5a. The powders are maintained in contact with the MB dye for 120 min before the photocatalytic test to eliminate the adsorptive effects. The first order kinetic constant was estimated using the linearization of concentration curves for a better measurement of photocatalytic activity, as shown in Fig. 5b [68].

It can be observed in Fig. 5a that only the CuO/ZnO heterostructure completely reduces the MB concentration after 80 min, while the bare samples reduce the MB concentration by 93% and 24% for ZnO and CuO, respectively. From the linearization data, kinetic constants *k* of 0.0031, 0.0258, 0.0573 and 0.0006 min^{-1} were obtained for CuO, ZnO, CuO–ZnO and photolysis samples, respectively. Thus, the formation of the CuO–ZnO heterostructure more than doubles the catalytic efficiency of ZnO. As previously discussed, ZnO powders have an E_{gap} of 3.25 eV, while CuO powders have 1.51 eV. Thus, the energy required for excitation of the electron from valence to conduction band is much lower for CuO. One of the main factors which determines the photocatalytic efficiency of semiconductor materials is preventing the recombination of photogenerated pairs (e^-/h^+) during the process, so that they act to produce species with high oxidative capacity of organic molecules. The lower E_{gap} for CuO enables a favored recombination for the photogenerated e^-/h^+ pairs during the catalytic process, while ZnO has a higher energy barrier.

On the other hand, the formation of the CuO/ZnO heterostructure acts with CuO (p-type) capturing the solar radiation and its excited electrons migrate to the ZnO (n-type) conduction band, performing reduction reactions and generating superoxide species [69]. Moreover, the electron decay from the ZnO conduction band to the CuO valence band is difficult, allowing the holes present in it to act in generating oxidation reactions, which in turn promote the formation of $^{\bullet}OH$ and H_2O_2 species with high degradation capacity of organic pollutants [70]. Thus, the heterojunction formed by the CuO and ZnO particles acts to prevent recombination of photo-generated pairs, allowing a superior generation rate of oxidative species.

In order to clarify the role of different photo-induced mechanism (photocatalysis and photolysis), the change in optical absorption spectra of MB dye photodegradation in the presence of a CuO/ZnO heterostructure under sunlight radiation for different time intervals were investigated, as shown in Fig. 6(a-d).

In Fig. 6 (a-c) it can be seen that the disappearance of the band at 664 nm indicates that MB has been photodegraded within 80 min and the corresponding C/C_0 values were reached at zero, which clearly indicates the complete degradation of dye solution in the presence of CuO, ZnO and CuO/ZnO heterostructure. On the other hand, in Fig. 6d it was noted that the optical absorption spectra of MB dye remains unchanged in the absence of investigated semiconductors, indicating

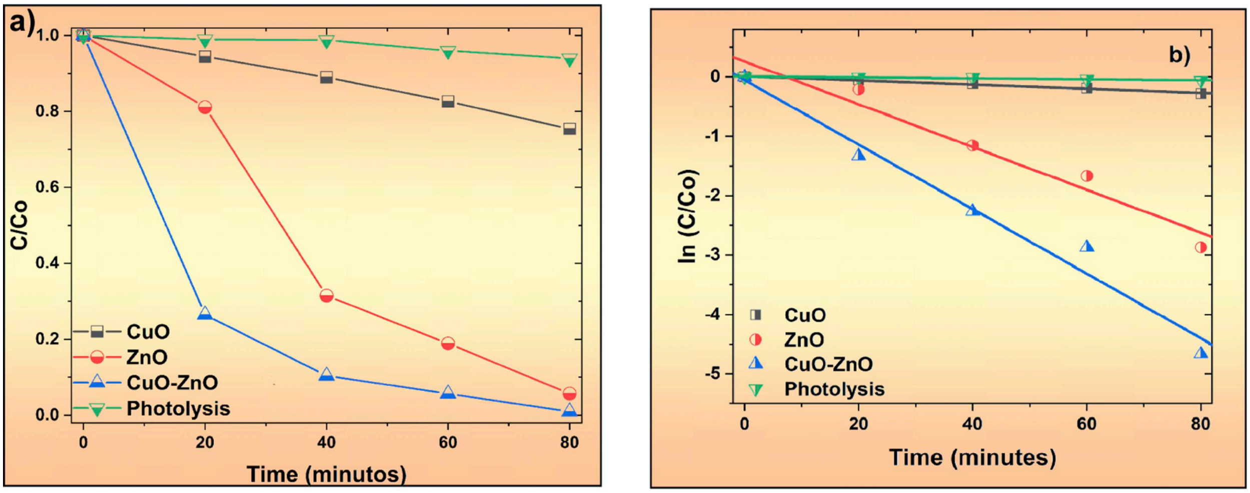

Fig. 5. **(a)** Plot of (Ct/C_0) as a function of irradiation time for MB degradation under sunlight and **(b)** linearization of Ct/C_0 curves for the kinetic constant (*k*) determination.

that the photolysis does not contribute to the overall MB photodegradation.

Theoretical calculations based on quantum mechanics were carried out in order to characterize and support a new interpretation of photocatalytic mechanism of the degradation of MB under visible-light irradiation in aiming to gain a deeper insight about the superior photocatalytic properties of theCuO/ZnO heterostructure.

3.1. DFT calculations

The optimized unit cells depicted in Fig. 7 were evaluated regarding the structural parameters and the building clusters in order to evaluate the crystalline structure for both p-CuO and n-ZnO oxides.

The optimized lattice parameters for wurtzite n-ZnO were a = b = 3.231 Å and c = 5.172 Å (V = 46.75 Å^3), while the [ZnO_4] clusters were obtained as a distorted tetrahedral center with three short Zn–O bonds of 1.963 Å and one larger of 1.973 Å, being in good agreement with previous theoretical and experimental results [71–73]. On the other hand, the optimized lattice parameters for the monoclinic p-CuO were found to be a = 4.429 Å, b = 3.701 Å and c = 5.157 Å (V = 84.34 Å^3), while the β value was obtained as 93.86°, being in reasonable agreement with experimental results and previous theoretical calculations [53,74]. In addition, a slight distortion along the square-planar arrangement was observed for the [CuO_4] cluster resulting in two distinct Cu–O bonds of 1.936 and 1.940 Å, corresponding to short and long paths, respectively. Raman frequencies were

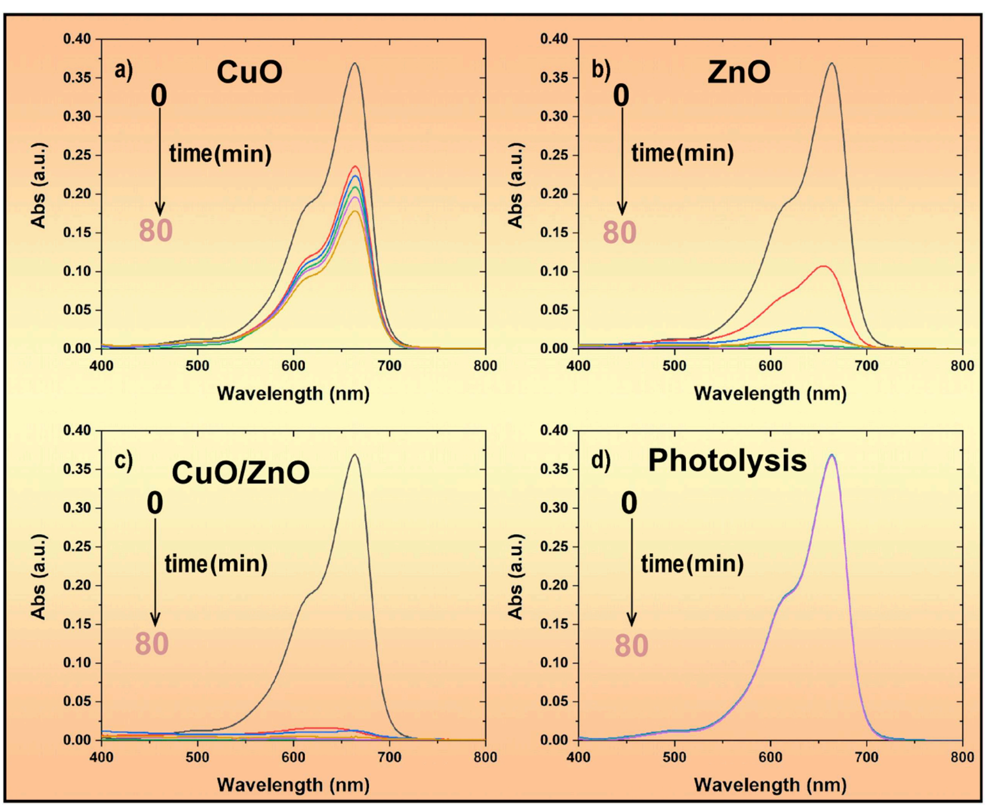

Fig. 6. Photodegradation of **(a)** CuO, **(b)** ZnO, **(c)** CuO/ZnO hetereostrucutre and **(d)** photolysis for different exposure times under sunlight radiation.

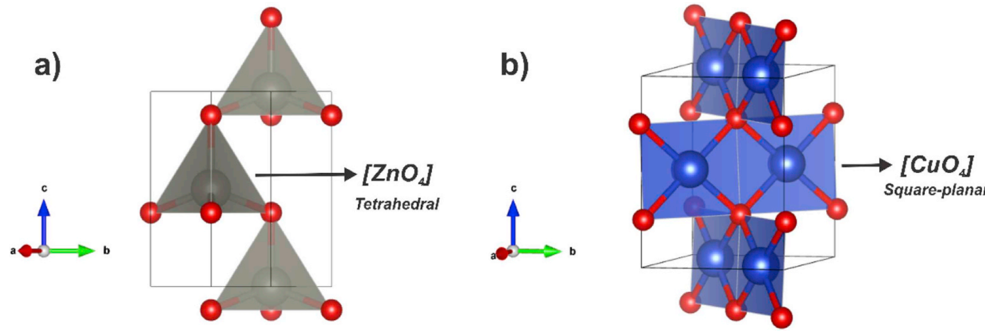

Fig. 7. Optimized unit cell for **(a)** n-ZnO and **(b)** p-CuO materials. Gray, Blue and Red balls correspond to Zn, Cu and O atoms. The building clusters are highlighted in both cases.

calculated and compared to previous theoretical [71] and experimental [75,76] results (Supplementary Information – Table S1) in order to verify the accuracy of the DFT/B1WC description for both p-CuO and n-ZnO oxides, evidencing a remarkable agreement which validates the optimized model.

Table S1

The electronic structure of both p-CuO and n-ZnO oxides are presented in Fig. 8. For the p-type CuO oxide (Fig. 8a), the DOS profiles indicate that the valence band is composed by O (2p) states hybridized with Cu (3d) orbitals, with the valence band maximum (VBM) being composed by half-filled $3d_{z}^{2}$ forming Cu–O bond paths along the c-axis. On the other hand, the conduction band was calculated to mainly be composed by the empty states from Cu (3d). Indeed, the conduction band minimum (CBM) shows a well-localized state corresponding to the empty $3d_{z}^{2}$ orbital hybridized with O (2p). In this case, the band-gap was calculated as 1.30 eV, being an indirect electronic excitation

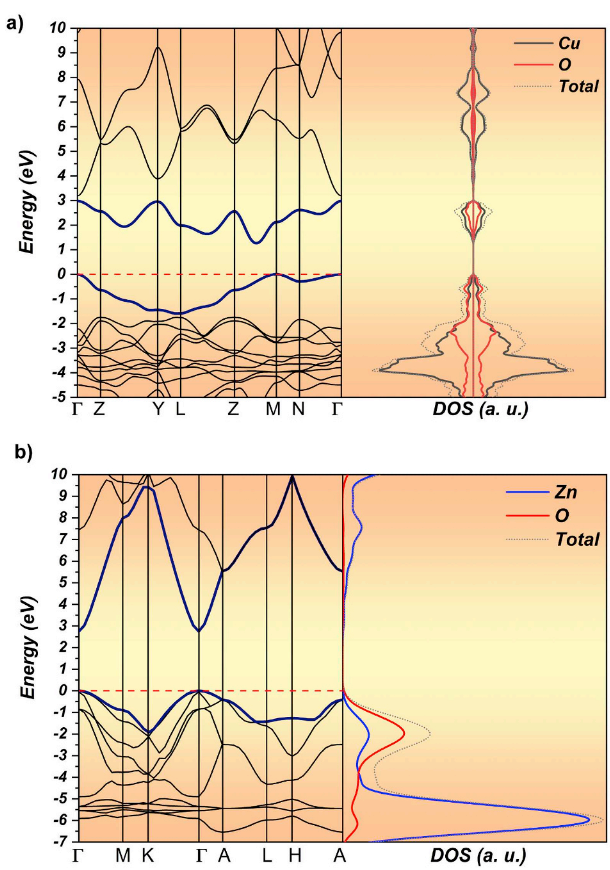

Fig. 8. Band Structure profiles and atom-resolved Density of States for **(a)** p-CuO and **(b)** n-ZnO materials. The Fermi level was set to zero in all cases.

involving the O (2p) electrons located at M point to the empty Cu $3d_{z}^{2}$ orbital localized between the Z-M *k*-points. The obtained band-gap value here was found to be in agreement with the experimental measures (1.51 eV – Fig. 4.). Previous theoretical studies carried out for tenorite p-CuO present band-gap values in the range of 1.5–3.0 eV, depending on the exchange-correlation treatment used in the theoretical calculations due to the challenging behavior of strongly correlated materials [53]. Thus, the electronic structure calculated for p-CuO indicates that hybrid B1WC can be used to simulate strongly correlated oxides, confirming the previous prediction for CeO_2 and Ce_2O_3 [54,55].

The DOS profiles for n-ZnO (Fig. 8b) indicate that the valence band is composed by O (2p) states hybridized with Zn; on the other hand, the conduction band was calculated to be mainly composed by the empty states from Zn. The calculated band-gap values in this case were 2.75 eV, which is in agreement with experimental results reported in this work (3.25 eV - Fig. 4) and other theoretical studies [71].

In aiming to disclose the superior photocatalytic behavior of CuO/ZnO heterostructure, we propose a DFT-based theoretical Z-scheme to schematically represent the band edge alignment of the CuO/ZnO system, as depicted in Fig. 9, computing the valence and conduction band edge by High-throughput DFT/B1WC calculations as proposed in previous theoretical studies for similar heterostructures [77].

Despite the experimental efforts to investigate the electronic structure of CuO/ZnO heterostructure [78–81], there are no theoretical studies focused on the description of the electronic aspects associated with the electronic excitation which generates the electron-hole pair responsible for the photocatalytic properties. Using a theoretical calculation, Naseri et al. [80] proposed that the mixed $Zn_{1-x}Cu_xO$ oxide shows a reduced band-gap value in comparison to the pristine ZnO, confirming that the creation of CuO/ZnO heterostructure is suitable due to the creation of intermediary energy levels in the band-gap region of ZnO which justify the band alignment. However, additional features associated with the nature of the excited e'-h$^{\bullet}$ pair remain unclear.

In this work, the electronic excitation is interpreted from the equation of defects based on the Kröger-Vink notation [82]. In this

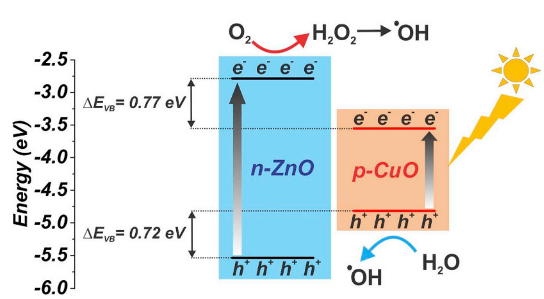

Fig. 9. Schematic band edge alignment of the CuO/ZnO heterostructure based on DFT/B1WC electronic structure calculations. In addition, the proposed mechanism of charge transfer under sunlight irradiation as well as the intermediate reactions for radical generation are highlighted.

nomenclature, the superscript x, 'and $^{\bullet}$ index indicates the existence of neutral, negative and positive charged clusters, respectively. First, the electrons located on the VB of CuO are excited under sunlight irradiation to the CB, generating an electron-hole pair located on the constituent $[CuO_4]$ clusters, as follows:

$$[CuO_4]^x + h\nu \rightarrow [CuO_4]'_{CB} + [CuO_4]^{\cdot}_{VB} \tag{1}$$

However, the band alignment depicted in Fig. 9 enables the photoexcited electrons in the p-type CuO conduction band to be transferred to the n-type ZnO conduction band. However, the constituent clusters in the exposed ZnO surfaces exhibit oxygen vacancies originated from the cleavage process, resulting in the generation of reduced $[ZnO_n]'$ species in the following reaction:

$$[ZnO_{4-n}...nV_O]^x_{CB} + [CuO_4]'_{CB} \rightarrow [ZnO_{4-n}...nV_O]'_{CB} + [CuO_4]^x_{CB} \tag{2}$$

In the next step, the presence of reduced $[ZnO_n]'$ species induces the adsorption of O_2 to generate H_2O_2 through a reaction channel in which free electrons are removed from the system. Thus, hydroxyl radicals are produced from hydrogen peroxide:

$$[ZnO_{4-n}...nV_O]'_{CB} + O_2 + 2H^+ \rightarrow [ZnO_{4-n}...nV_O]^x_{CB} + H_2O_2 \tag{3}$$

$$H_2O_2 \rightarrow 2^{\cdot}OH \tag{4}$$

On the other hand, the holes located on the exposed under-coordinated clusters located at VB of n-type ZnO can be transferred to p-type CuO VB, where they can react with adsorbed water to generate additional hydroxyl radicals, following the reaction:

$$[CuO_{4-n}...nV_O]^x_{VB} + [ZnO_{4-n}...nV_O]^{\cdot}_{VB} \rightarrow [CuO_{4-n}...nV_O]^{\cdot}_{VB} + [ZnO_{4-n}...nV_O]^x_{VB} \tag{5}$$

$$[CuO_{4-n}...nV_O]^{\cdot}_{VB} + H_2O \rightarrow H^{\cdot} + {}^{\cdot}OH \tag{6}$$

In this context, the originated hydroxyl radicals can react with the organic structure of the MB dye in a degradation reaction which generates CO_2 and H_2O molecules, following:

$$MB + {}^{\cdot}OH \rightarrow intermediates \rightarrow CO_2 + H_2O \tag{7}$$

Therefore, the proposed mechanism (Eqs. (1)–(7)) follows previous experimental evidence based on CuO/ZnO heterostructures and similar p/n heterojunctions [80,83,84]. Furthermore, the obtained results indicate that as-produced hydroxyl radicals can lead to effective degradation of MB. This fact can be confirmed by the inclusion of additional H_2O_2 which contributes to the reaction mechanism (Eq. (5)) to generate additional hydroxyl radicals which in turn accelerates the degradation of MB, as previously reported in the experimental results.

Therefore, in combining photocatalysis measurements and theoretical DFT calculations, the degradation mechanism of MB by CuO/ZnO heterostructure was accurately disclosed, confirming that the optimized heterostructure reported in this study can be a good candidate for effective removal of environmental pollutants.

4. Conclusions

In summary, CuO/ZnO heterostructures were successfully synthesized using a facile microwave-assisted hydrothermal methodology and its geometry, electronic structure and photocatalytic performance were analyzed by combining experimental techniques and theoretical calculations. XRD patterns and FE-SEM analysis confirmed the formation of CuO/ZnO heterostructure showing a mixed architecture based on simple oxide constituents. When employed as photocatalysts, the as-synthesized CuO/ZnO heterostructure exhibited excellent activity in the degradation MB dye under solar radiation. The enhanced photocatalysis was discussed based on DFT calculations of a Z-scheme to schematically represent the band edge alignment of the CuO/ZnO system. In this case, the reduced E_{gap} for p-type CuO enhances the solar-driven electron excitation, while the energy levels of n-type ZnO induces a separation of photo-generated charge carriers, resulting in a reduced recombination rate. Therefore, such carriers combined with the undercoordinated clusters presented along the CuO and ZnO surfaces can act in generating radical species which act along the MB dye degradation. Thus, this study provides new insight into the design and fabrication of highly efficient p-n junction hetero nanostructures with enhanced photocatalytic activity based on the molecular interpretation of the main fingerprints associated with the photo-induced mechanism.

Declaration of competing interest

The authors declare that they have no known competing financial interests or personal relationships that could have appeared to influence the work reported in this paper.

Acknowledgements

The authors gratefully acknowledge the financial support from the *CAPES Finance Code 001*, *CNPq*, *FAPESP* (2013/07296-2), the Federal University of Rio Grande do Norte (PPGCEM-UFRN), Federal University of São Carlos and State University of Ponta Grossa. M. C. Oliveira acknowledges the financial support from *PNPD/CAPES* (88887.319041/2019–00). R. A. P. Ribeiro acknowledges financial support from *CNPq* (156176/2018-1).

Appendix A. Supplementary data

Supplementary data to this article can be found online at https://doi.org/10.1016/j.ceramint.2019.12.205.

References

[1] T. Soejima, K. Takada, S. Ito, Alkaline vapor oxidation synthesis and electrocatalytic activity toward glucose oxidation of CuO/ZnO composite nanoarrays, Appl. Surf. Sci. 277 (2013) 192–200.
[2] M. Mansournia, L. Ghaderi, CuO@ZnO core-shell nanocomposites: novel hydrothermal synthesis and enhancement in photocatalytic property, J. Alloy. Comp. 691 (2017) 171–177.
[3] B. Li, Y. Wang, Facile synthesis and photocatalytic activity of ZnO–CuO nanocomposite, Superlattice Microstruct. 47 (2010) 615–623.
[4] M. Prabhu, J. Mayandi, R.N. Mariammal, V. Vishnukanthan, J.M. Pearce, N. Soundararajan, K. Ramachandran, Peanut shaped ZnO microstructures: controlled synthesis and nucleation growth toward low-cost dye sensitized solar cells, Mater. Res. Express 2 (2015) 066202.
[5] Z. Zang, Efficiency enhancement of ZnO/Cu_2O solar cells with well oriented and micrometer grain sized Cu2O films, Appl. Phys. Lett. 112 (2018) 042106.
[6] S. Joshi, R.K CB, L.A. Jones, E.L.H. Mayes, S.J. Ippolito, M.V. Sunkara, Modulating interleaved ZnO assembly with CuO nanoleaves for multifunctional performance: perdurable CO_2 gas sensor and visible light catalyst, Inorg. Chem. Front. 4 (2017) 1848–1861.
[7] F.-X. Liang, Y. Gao, C. Xie, X.-W. Tong, Z.-J. Li, L.-B. Luo, Recent advances in the fabrication of graphene–ZnO heterojunctions for optoelectronic device applications, J. Mater. Chem. C 6 (2018) 3815–3833.
[8] R. Saravanan, S. Karthikeyan, V.K. Gupta, G. Sekaran, V. Narayanan, A. Stephen, Enhanced photocatalytic activity of ZnO/CuO nanocomposite for the degradation of textile dye on visible light illumination, Mater. Sci. Eng. C 33 (2013) 91–98.
[9] J. Bandara, U.W. Pradeep, R.G.S.J. Bandara, The role of n–p junction electrodes in minimizing the charge recombination and enhancement of photocurrent and photovoltage in dye sensitized solar cells, J. Photochem. Photobiol. A Chem. 170 (2005) 273–278.
[10] J.L. Noel, R. Udayabhaskar, B. Renganathan, S. Muthu Mariappan, D. Sastikumar, B. Karthikeyan, Spectroscopic and fiber optic ethanol sensing properties Gd doped ZnO nanoparticles, Spectrochim. Acta A Mol. Biomol. Spectrosc. 132 (2014) 634–638.
[11] A. Ghosh, N. Kumari, S. Tewari, A. Bhattacharjee, Structural, electrical and optical studies on ruthenium doped ZnO pellets for device applications, Mater. Sci. Eng., B 196 (2015) 7–14.
[12] A. Ohtomo, M. Kawasaki, T. Koida, K. Masubuchi, H. Koinuma, Y. Sakurai, Y. Yoshida, T. Yasuda, Y. Segawa, $Mg_xZn_{1-x}O$ as a II–VI widegap semiconductor alloy, Appl. Phys. Lett. 72 (1998) 2466–2468.
[13] S. Chatkaewsueb, N. Saysunee, N. Tamaekong, The synthesis and characterization of p-CuO/n-ZnO nanoparticles synthesized by chemical method, Mater. Today Proc. 4 (2017) 6111–6117.
[14] L. Tan, H. Gao, R.S. Andriamitantsoa, B.-t. Hu, Facial fabrication of hierarchical 3D Sisal-like CuO/ZnO nanocomposite and its catalytic properties, Chem. Phys. Lett. 708 (2018) 77–80.

[15] S.P. Mardikar, S. Kulkarni, P.V. Adhyapak, Sunlight driven highly efficient degradation of methylene blue by CuO-ZnO nanoflowers, J. Environ. Chem. Eng. (2018) In press.
[16] S.F. Resende, J.A.R. Teodoro, I. Binatti, R.L. Gouveia, B.S. Oliveira, R. Augusti, On-surface photocatalytic degradation of methylene blue: in situ monitoring by paper spray ionization mass spectrometry, Int. J. Mass Spectrom. 418 (2017) 107–111.
[17] J. Lin, Z. Luo, J. Liu, P. Li, Photocatalytic degradation of methylene blue in aqueous solution by using ZnO-SnO_2 nanocomposites, Mater. Sci. Semicond. Process. 87 (2018) 24–31.
[18] F. Azeez, E. Al-Hetlani, M. Arafa, Y. Abdelmonem, A.A. Nazeer, M.O. Amin, M. Madkour, The effect of surface charge on photocatalytic degradation of methylene blue dye using chargeable titania nanoparticles, Sci. Rep. 8 (2018) 7104.
[19] X.-M. Song, C. Yuan, Y. Wang, B. Wang, H. Mao, S. Wu, Y. Zhang, ZnO/CuO photoelectrode with n-p heterogeneous structure for photoelectrocatalytic oxidation of formaldehyde, Appl. Surf. Sci. 455 (2018) 181–186.
[20] C. Yang, W. Dong, G. Cui, Y. Zhao, X. Shi, X. Xia, B. Tang, W. Wang, Highly-efficient photocatalytic degradation of methylene blue by PoPD-modified TiO2nanocomposites due to photosensitization-synergetic effect of TiO_2 with PoPD, Sci. Rep. 7 (2017) 3973.
[21] R.S. Dariani, A. Esmaeili, A. Mortezaali, S. Dehghanpour, Photocatalytic reaction and degradation of methylene blue on TiO_2 nano-sized particles, Optik 127 (2016) 7143–7154.
[22] M. Xue, L. Huang, J.-Q. Wang, Y. Wang, L. Gao, J.-h. Zhu, Z.-G. Zou, The direct synthesis of mesoporous structured MnO_2/TiO_2 nanocomposite: a novel visible-light active photocatalyst with large pore size, Nanotechnology 19 (2008) 185604.
[23] M. Long, W. Cai, J. Cai, B. Zhou, X. Chai, Y. Wu, Efficient photocatalytic degradation of phenol over $Co_3O_4/BiVO_4$ composite under visible light irradiation, J. Phys. Chem. B 110 (2006) 20211–20216.
[24] G. Li, N.M. Dimitrijevic, L. Chen, T. Rajh, K.A. Gray, Role of surface/interfacial Cu^{2+} sites in the photocatalytic activity of coupled $CuO-TiO_2$ nanocomposites, J. Phys. Chem. C 112 (2008) 19040–19044.
[25] Y. He, Z. Wu, L. Fu, C. Li, Y. Miao, L. Cao, H. Fan, B. Zou, Photochromism and size effect of WO_3 and WO_3-TiO_2 aqueous sol, Chem. Mater. 15 (2003) 4039–4045.
[26] K.Y. Song, M.K. Park, Y.T. Kwon, H.W. Lee, W.J. Chung, W.I. Lee, Preparation of transparent particulate MoO_3/TiO_2 and WO_3/TiO_2 films and their photocatalytic properties, Chem. Mater. 13 (2001) 2349–2355.
[27] G. Marcì, V. Augugliaro, M.J. López-Muñoz, C. Martín, L. Palmisano, V. Rives, M. Schiavello, R.J.D. Tilley, A.M. Venezia, Preparation characterization and photocatalytic activity of polycrystalline ZnO/TiO_2 systems. 1. Surface and bulk characterization, J. Phys. Chem. B 105 (2001) 1026–1032.
[28] J. Bandara, S.S. Kuruppu, U.W. Pradeep, The promoting effect of MgO layer in sensitized photodegradation of colorants on TiO_2/MgO composite oxide, Colloid. Surf. Physicochem. Eng. Asp. 276 (2006) 197–202.
[29] P. Senthil Kumar, M. Selvakumar, S. Ganesh Babu, S. Induja, S. Karuthapandian, CuO/ZnO nanorods: an affordable efficient p-n heterojunction and morphology dependent photocatalytic activity against organic contaminants, J. Alloy. Comp. 701 (2017) 562–573.
[30] J.H. Zeng, B.B. Jin, Y.F. Wang, Facet enhanced photocatalytic effect with uniform single-crystalline zinc oxide nanodisks, Chem. Phys. Lett. 472 (2009) 90–95.
[31] Y. Chen, H. Zhao, B. Liu, H. Yang, Charge separation between wurtzite ZnO polar {001} surfaces and their enhanced photocatalytic activity, Appl. Catal. B Environ. 163 (2015) 189–197.
[32] F. Lu, W. Cai, Y. Zhang, ZnO hierarchical micro/nanoarchitectures: solvothermal synthesis and structurally enhanced photocatalytic performance, Adv. Funct. Mater. 18 (2008) 1047–1056.
[33] C. Ye, Y. Bando, G. Shen, D. Golberg, Thickness-Dependent photocatalytic performance of ZnO nanoplatelets, J. Phys. Chem. B 110 (2006) 15146–15151.
[34] A. Zaoui, M. Ferhat, R. Ahuja, Magnetic properties of (ZnO)1/(CuO)1 (001) superlattice, Appl. Phys. Lett. 94 (2009) 102102.
[35] D. Zhang, Synthesis and characterization of ZnO-doped cupric oxides and evaluation of their photocatalytic performance under visible light, Transit. Met. Chem. 35 (2010) 689–694.
[36] L. Wang, Y. Kang, Y. Wang, B. Zhu, S. Zhang, W. Huang, S. Wang, CuO nanoparticle decorated ZnO nanorod sensor for low-temperature H2S detection, Mater. Sci. Eng. C 32 (2012) 2079–2085.
[37] Y.-F. Lim, C.S. Chua, C.J.J. Lee, D. Chi, Sol–gel deposited Cu_2O and CuO thin films for photocatalytic water splitting, Phys. Chem. Chem. Phys. 16 (2014) 25928–25934.
[38] Y.J. Jang, J.-W. Jang, S.H. Choi, J.Y. Kim, J.H. Kim, D.H. Youn, W.Y. Kim, S. Han, J. Sung Lee, Tree branch-shaped cupric oxide for highly effective photoelectrochemical water reduction, Nanoscale 7 (2015) 7624–7631.
[39] X.Y. Fan, Z.G. Wu, P.X. Yan, B.S. Geng, H.J. Li, C. Li, P.J. Zhang, Fabrication of well-ordered CuO nanowire arrays by direct oxidation of sputter-deposited Cu3N film, Mater. Sci. Eng. B 62 (2008) 1805–1808.
[40] J. Gajendiran, V. Rajendran, Synthesis and characterization of coupled semiconductor metal oxide (ZnO/CuO) nanocomposite, Mater. Lett. 116 (2014) 311–313.
[41] Z.-L. Liu, J.-C. Deng, J.-J. Deng, F.-F. Li, Fabrication and photocatalysis of CuO/ZnO nano-composites via a new method, Mater. Sci. Eng. B 150 (2008) 99–104.
[42] R.K. Sharma, R. Ghose, Synthesis of nanocrystalline CuO–ZnO mixed metal oxide powder by a homogeneous precipitation method, Ceram. Int. 40 (2014) 10919–10926.
[43] M.H. Habibi, B. Karimi, Application of impregnation combustion method for fabrication of nanostructure CuO/ZnO composite oxide: XRD, FESEM, DRS and FTIR study, J. Ind. Eng. Chem. 20 (2014) 1566–1570.
[44] L.S.R. Rocha, C.R. Foschini, C.C. Silva, E. Longo, A.Z. Simões, Novel ozone gas sensor based on ZnO nanostructures grown by the microwave-assisted hydrothermal route, Ceram. Int. 42 (2016) 4539–4545.
[45] K. Ocakoglu, S.A. Mansour, S. Yildirimcan, A.A. Al-Ghamdi, F. El-Tantawy, F. Yakuphanoglu, Microwave-assisted hydrothermal synthesis and characterization of ZnO nanorods, Spectrochim. Acta: Mol. Biomol. Spectrosc. 148 (2015) 362–368.
[46] L.-Y. Meng, B. Wang, M.-G. Ma, K.-L. Lin, The progress of microwave-assisted hydrothermal method in the synthesis of functional nanomaterials, Mater. Today Chem. 1–2 (2016) 63–83.
[47] B.D. Viezbicke, S. Patel, B.E. Davis, D.P. Birnie III, Evaluation of the Tauc method for optical absorption edge determination: ZnO thin films as a model system, Phys. Status Solidi B 252 (2015) 1700–1710.
[48] R. Dovesi, A. Erba, R. Orlando, C.M. Zicovich-Wilson, B. Civalleri, L. Maschio, M. Rérat, S. Casassa, J. Baima, S. Salustro, B. Kirtman, Quantum-mechanical condensed matter simulations with CRYSTAL, 0, Wiley Interdiscip. Rev.: Comput. Mol. Sci. 8 (2018) e1360.
[49] T. Bredow, K. Jug, R.A. Evarestov, Electronic and magnetic structure of ScMnO3, Phys. Status Solidi 243 (2006) R10–R12.
[50] J.E. Jaffe, A.C. Hess, Hartree-Fock study of phase changes in ZnO at high pressure, Phys. Rev. B 48 (1993) 7903–7909.
[51] K. Doll, N.M. Harrison, Chlorine adsorption on the Cu(111) surface, Chem. Phys. Lett. 317 (2000) 282–289.
[52] G. Drera, A. Giampietri, A. Febbrari, M. Patrini, M.C. Mozzati, L. Sangaletti, Band offset and gap tuning of tetragonal CuO-$SrTiO_3$ heterojunctions, Phys. Rev. B 99 (2019) 075124.
[53] M. Heinemann, B. Eifert, C. Heiliger, Band structure and phase stability of the copper oxides Cu_2O, CuO and Cu_4O_3, Phys. Rev. B 87 (2013) 115111.
[54] L. Brugnoli, A.M. Ferrari, B. Civalleri, A. Pedone, M.C. Menziani, Assessment of density functional approximations for highly correlated oxides: the case of CeO_2 and Ce_2O_3, J. Chem. Theory Comput. 14 (2018) 4914–4927.
[55] J. Graciani, A.M. Márquez, J.J. Plata, Y. Ortega, N.C. Hernández, A. Meyer, C.M. Zicovich-Wilson, J.F. Sanz, Comparative study on the performance of hybrid DFT functionals in highly correlated oxides: the case of CeO_2 and Ce_2O_3, J. Chem. Theory Comput. 7 (2011) 56–65.
[56] H.J. Monkhorst, J.D. Pack, Special points for Brillouin-zone integrations, Phys. Rev. B 13 (1976) 5188–5192.
[57] D.P. Volanti, M.O. Orlandi, J. Andrés, E. Longo, Efficient microwave-assisted hydrothermal synthesis of CuO sea urchin-like architectures via a mesoscale self-assembly, CrystEngComm 12 (2010) 1696–1699.
[58] C. Florica, A. Costas, A.G. Boni, R. Negrea, L. Ion, N. Preda, L. Pintilie, I. Enculescu, Electrical properties of single CuO nanowires for device fabrication: diodes and field effect transistors, Appl. Phys. Lett. 106 (2015) 223501.
[59] S. Asbrink, A. Waskowska, CuO: X-ray single-crystal structure determination at 196 K and room temperature, J. Phys. Condens. Matter 3 (1991) 8173–8180.
[60] J. Albertsson, S.C. Abrahams, A. Kvick, Atomic displacement, anharmonic thermal vibration, expansivity and pyroelectric coefficient thermal dependences in ZnO, Acta Crystallogr. B 45 (1989) 34–40.
[61] L. Xu, S. Sithambaram, Y. Zhang, C.-H. Chen, L. Jin, R. Joesten, S.L. Suib, Novel urchin-like CuO synthesized by a facile reflux method with efficient olefin epoxidation catalytic performance, Chem. Mater. 21 (2009) 1253–1259.
[62] P. Schemer, Bestimmung der Grosse und der Inneren Struktur von Kolloidteilchen Mittels Rontgenstrahlen, Nachrichten von der Gesellschaft der Wissenschaften, Gottingen, Math.-Phys. 2 (1918) 98–100.
[63] T.P. Yendrapati Taraka, A. Gautam, S.L. Jain, S. Bojja, U. Pal, Controlled addition of Cu/Zn in hierarchical CuO/ZnO p-n heterojunction photocatalyst for high photoreduction of CO_2 to MeOH, J. CO_2 Utilization 31 (2019) 207–214.
[64] L. Tolvaj, K. Mitsui, D. Varga, Validity limits of Kubelka–Munk theory for DRIFT spectra of photodegraded solid wood, Wood Sci. Technol. 45 (2011) 135–146.
[65] N.F. Andrade Neto, K.N. Matsui, C.A. Paskocimas, M.R.D. Bomio, F.V. Motta, Study of the photocatalysis and increase of antimicrobial properties of Fe^{3+} and Pb^{2+} co-doped ZnO nanoparticles obtained by microwave-assisted hydrothermal method, Mater. Sci. Semicond. Process. 93 (2019) 123–133.
[66] N.F. Andrade Neto, P.M. Oliveira, R.M. Nascimento, C.A. Paskocimas, M.R.D. Bomio, F.V. Motta, Influence of pH on the morphology and photocatalytic activity of CuO obtained by the sonochemical method using different surfactants, Ceram. Int. 45 (2019) 651–658.
[67] M.A. Bajiri, A. Hezam, K. Namratha, R. Viswanath, Q.A. Drmosh, H.S. Bhojya Naik, K. Byrappa, CuO/ZnO/g-C_3N_4 heterostructures as efficient visible light-driven photocatalysts, J. Environ. Chem. Eng. 7 (2019) 103412.
[68] N.F. Andrade Neto, P.M. Oliveira, M.R.D. Bomio, F.V. Motta, Effect of temperature on the morphology and optical properties of Ag2WO4 obtained by the co-precipitation method: photocatalytic activity, Ceram. Int. 45 (2019) 15205–15212.
[69] T.P. Yendrapati Taraka, A. Gautam, S.L. Jain, S. Bojja, U. Pal, Controlled addition of Cu/Zn in hierarchical CuO/ZnO p-n heterojunction photocatalyst for high photoreduction of CO2 to MeOH, J. CO2 Utilization 31 (2019) 207–214.
[70] S. Paul, J. Sultana, A. Bhattacharyya, A. Karmakar, S. Chattopadhyay, Investigation of the comparative photovoltaic performance of n-ZnO nanowire/p-Si and n-ZnO nanowire/p-CuO heterojunctions grown by chemical bath deposition method, Optik 164 (2018) 745–752.
[71] N.L. Marana, S.M. Casassa, J.R. Sambrano, Piezoelectric, elastic, Infrared and Raman behavior of ZnO wurtzite under pressure from periodic DFT calculations, Chem. Phys. 485–486 (2017) 98–107.
[72] M. Catti, Y. Noel, R. Dovesi, Full piezoelectric tensors of wurtzite and zinc blende ZnO and ZnS by first-principles calculations, J. Phys. Chem. Solids 64 (2003) 2183–2190.
[73] F. Decremps, F. Datchi, A.M. Saitta, A. Polian, S. Pascarelli, A. Di Cicco, J.P. Itié, F. Baudelet, Local structure of condensed zinc oxide, Phys. Rev. B 68 (2003)

104101.
[74] L. Debbichi, M.C. Marco de Lucas, J.F. Pierson, P. Krüger, Vibrational properties of CuO and Cu_4O_3 from first-principles calculations, and Raman and infrared spectroscopy, J. Phys. Chem. C 116 (2012) 10232–10237.
[75] F. Decremps, J. Pellicer-Porres, A.M. Saitta, J.-C. Chervin, A. Polian, High-pressure Raman spectroscopy study of wurtzite ZnO, Phys. Rev. B 65 (2002) 092101.
[76] G. Kliche, Z.V. Popovic, Far-infrared spectroscopic investigations on CuO, Phys. Rev. B 42 (1990) 10060–10066.
[77] L.H.d.S. Lacerda, S.R. de Lazaro, Isomorphic substitution and intermediary energy levels: a new application of DFT modelling and semiconductor theory to describe p–n type junctions interface in heterostructures, Phys. Status Solidi (b) (2017) 254 1700119.
[78] H. Fang, Y. Guo, T. Wu, Y. Liu, Biomimetic synthesis of urchin-like CuO/ZnO nanocomposites with excellent photocatalytic activity, New J. Chem. 42 (2018) 12779–12786.
[79] F. Cao, T. Wang, X. Ji, Enhanced visible photocatalytic activity of tree-like ZnO/CuO nanostructure on Cu foam, Appl. Surf. Sci. 471 (2019) 417–424.
[80] A. Naseri, M. Samadi, N.M. Mahmoodi, A. Pourjavadi, H. Mehdipour, A.Z. Moshfegh, Tuning composition of electrospun ZnO/CuO nanofibers: toward controllable and efficient solar photocatalytic degradation of organic pollutants, J. Phys. Chem. C 121 (2017) 3327–3338.
[81] D. Malwal, P. Gopinath, CuO-ZnO nanosheets with p–n heterojunction for enhanced visible light mediated photocatalytic activity, ChemistrySelect 2 (2017) 4866–4873.
[82] F.A. Kröger, H.J. Vink, Relations between the concentrations of imperfections in crystalline solids, in: F. Seitz, D. Turnbull (Eds.) Solid State Physics, Academic Press1956, pp. 307-435.
[83] S. Joshi, R.K. Canjeevaram Balasubramanyam, S.J. Ippolito, Y.M. Sabri, A.E. Kandjani, S.K. Bhargava, M.V. Sunkara, Straddled band Aligned CuO/$BaTiO_3$ heterostructures: role of energetics at nanointerface in improving photocatalytic and CO_2 sensing performance, ACS Appl. Nano Mater. 1 (2018) 3375–3388.
[84] Z. Li, X. Pan, Z. Yi, Photocatalytic oxidation of methane over CuO-decorated ZnO nanocatalysts, J. Mater. Chem. 7 (2019) 469–475.